A METHODOLOGY FOR LINEARIZATION OF HIGHLY COUPLED ROTOR-BODY DYNAMICS FOR SIDE-BY-SIDE HELICOPTERS

Francesco Mazzeo, University of Modena and Reggio Emilia, Modena (MO), Italy

Marilena D. Pavel, Delft University of Technology, The Netherlands

Francesco Leali, University of Modena and Reggio Emilia, Modena (MO), Italy

Fabrizio Giulietti, University of Bologna, Forlì (FC), Italy

Abstract

This paper presents a 38-state space linear flight dynamics representation of a side-by-side helicopter. The aim of the paper is to propose an original linearization and trim methodology to deal with highly complex numerical mathematical models involving coupled flap and lead-lag rotor dynamics. The trim and stability features of the helicopter are computed by using this method and the effects of blade's flexibility on body flight dynamics are discussed. Rotorcraft's stability is governed by two unstable oscillatory modes, identified as typical phugoid and dutch-roll, and four real, stable, dynamics of different frequencies. The results show also that while the rotor lead-lag is beneficial for the overall stability, the lateral/longitudinal inflow modes destabilize the motion. The presented methodology allows furthermore to evaluate the impact of the rotor- body - couplings on vehicle characteristics and can be extended to investigate the stability of any vertical take-off and landing (VTOL) configuration.

Keywords

Simulation and modeling, side-by-side helicopter, flight dynamics, linearization, trim

1. INTRODUCTION

Modeling and simulation of different configurations of Vertical Take-Off and Landing (VTOL) vehicles in is a core subject when defining new concepts of Urban Air Mobility (UAM) ecosystems [1]. Different approaches have been developed to reproduce the flight and rotor blade dynamics of rotary wing systems such as helicopters, drones and multirotors, with different levels of complexity. For example, a minimum complexity analytical model for helicopters was developed by Hefley [2] by assuming a rigid body subjected to forces and moments derived from general momentum theory and rotor flapping dynamics approximated by first order ordinary differential equations. A similar approach was adopted by Talbot [3], who developed an analytical model of the main rotor by assuming a second order dynamic flap and uniform dynamic inflow. Next, more complex approaches were formulated by using the principles of multi-body dynamics. This is the case of the commercial software FLIGHTLAB [4] and the aeroelastic analysis performed by Savino *et al.* [5] for rotary wing vehicles. More recently, the application of computational fluid dynamics (CFD) coupled with computational structural dynamics (CSD) solutions was considered, although this approach requires large computational costs [6].

An additional type of modeling technique, instead, adopts numerical differential equations for both helicopter and rotor blades motion. It is the case of GenHel [7], a nonlinear mathematical model of the UR-60A Black Hawk helicopter developed by NASA for flight dynamics and handling qualities evaluations. Similarly, Taamallah [8] presented a numerical representation of a small-scale helicopter for flight dynamics simulations and control system design. In his work, a coupled second order rotor dynamics including blade flap and lead lag motions is derived with a Lagrangian approach. However, the increasing complexity of the mathematical models leads to challenges in the derivation of a linear state-space representation of the rotorcraft system. In particular, the increased level of time-dependency and coupling between rotor and rigid body modes, makes the classical linearization methods [9] not suitable for this type of formulations. Although numerical models present the advantage of a higher fidelity in the representation of the body and single blade motion, when it comes to linearization, numerical issues appear. In particular, three issues can be identified when linearizing complex nonlinear dynamic helicopter models:

1. linearizing equations in a rotating frame system provides a loss of physical meaning of the tip-path plane and rotor center of gravity dynamics;

2. a strong coupling between flap and lead-lag dynamics makes the isolation of the two effects impractical;

3. complex, nonlinear terms in the equations are derived from a numerical integration of forces and moments along the blade, making the derivation of an analytical representation of the state matrix not feasible.

While most of the research analysis employs commercial and built-in software to investigate the rotor dynamics [10, 11], only few studies highlight the issues and procedures to produce a reliable linear state-space model to include the rotor dynamics and body-rotor coupling in the classical rigid-body representation [9, 12]. Nevertheless, none of them defines a clear methodology to deal with numerical representations.

The aim of the present paper is to provide the guidelines needed in linearizing complex numerical models and apply them to an innovative VTOL configuration. The case studied in this paper is a small-scale side-by-side helicopter, properly designed for UAM purposes by SABGroup s.r.l. [13] The paper provides a numerical formulation of such a configuration and study its trim and stability properties by applying the linearization method and understand the effects of blade flexibility on rotorcraft flight dynamics.

2. METHODS

2.1. Modelling

2.1.1 Modelling overview and case study

The VTOL studied in this work is a symmetric, small-scale, side-by-side helicopter depicted in Figure 1. Data of the helicopter are summarized in Table 6.

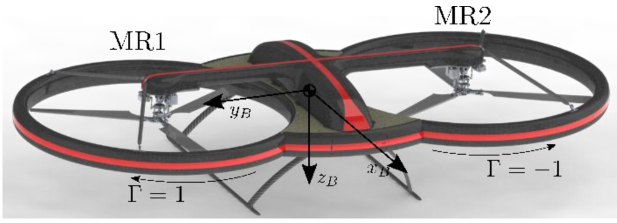

Figure 1: Small-scale side-by-side helicopter

The rotorcraft has two counter rotating, synchronous and ducted rotors, operating at constant angular speed and connected by a drive belt. Each rotor is actuated with a classical mechanical swashplate, and the single rotor controls (collective pitch, longitudinal and lateral cyclic) are mixed with each other to reduce the over actuation of the whole system to 4 global controls: a global collective pitch, equal in the two rotors, to control the vertical motion of the VTOL ($\theta_0 = \theta_0^{(1)} = \theta_0^{(2)}$); a global lateral cyclic for lateral movement ($A_{1s} = A_{1s}^{(1)} = A_{1s}^{(2)}$); a global longitudinal cyclic for forward movement ($B_{1s} = \frac{B_{1s}^{(1)}+B_{1s}^{(2)}}{2}$), providing an average longitudinal swashplate tilt in the two rotors; and a differential longitudinal cyclic control which exploits the elasticity of the blades to produce a yawing moment ($\Delta B_{1s} = \frac{B_{1s}^{(2)}-B_{1s}^{(2)}}{2}$).

A numerical mathematical model for rotorcraft flight dynamics including rotor blades dynamics, was developed to study the trim and VTOL stability. The formulation has 24 dof with the hypothesis of a rigid body moving on a flat and non-rotating Earth. A second-order coupled flap-lag dynamics is integrated into the main rotors representation. A non-uniform, first-order, dynamic inflow provided by Peters *et al.* [14] is assumed. The main rotors are modeled with a single-blade approach based on the blade element theory, where each blade is divided into a finite number of sections, whose forces and moments are integrated along the blade span to compute the rotor contribution at each time step. The fuselage aerodynamic loads are represented by a flat-plate approximation. A panel method implemented in the OpenVSP software, is adopted to calculate the parasite drag of the frontal, side and top equivalent areas and a simple analytical and continuous model is developed. A detailed description of the fuselage contribution is reported in Mazzeo *et al.* [15], as well as the shrouds effect.

The presence of the ducts is taken into account with the integration of semi-analytical results produced by Bourtsev et al. [16] and the Leishman representation of the thrust with ducted fans [17]. A schematic representation of the modeling framework is reported in Figure 2Figure 2. As remainder, for this paper's notations, the vectors are indicated with bold symbols, while capital letters are used to identify matrix terms in the equations, with the only exception of rotorcraft data summarized in Table 6.

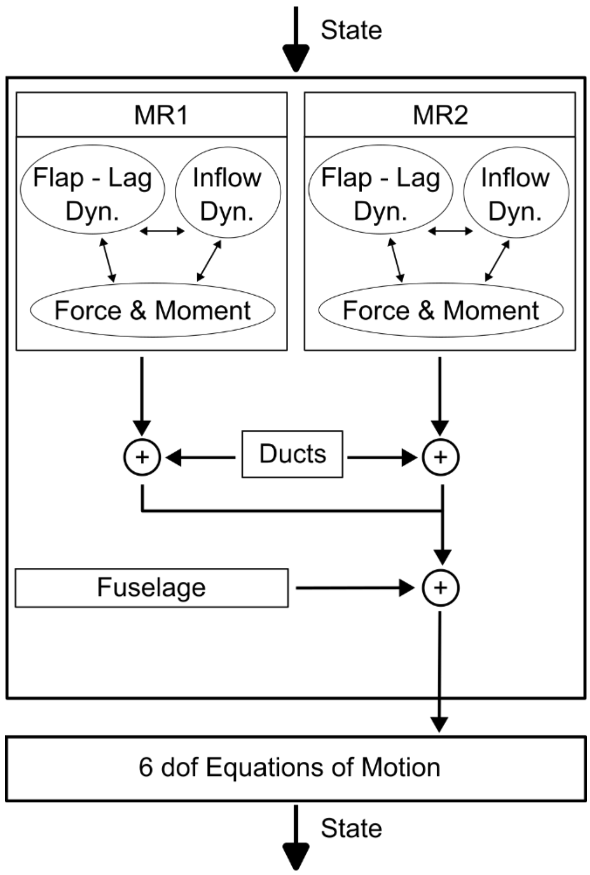

Figure 2: Modelling scheme for a side-by-side helicopter

According to this scheme, the total external force and moment acting on the rotorcraft are

[1] $\boldsymbol{F} = \boldsymbol{F}^{(1)} + \boldsymbol{F}^{(2)} + \boldsymbol{F}_{\boldsymbol{d}}^{(1)} + \boldsymbol{F}_{\boldsymbol{d}}^{(2)} + \boldsymbol{F}_{\boldsymbol{f}}$ and

[2] $\boldsymbol{M} = \boldsymbol{M}^{(1)} + \boldsymbol{M}^{(2)} + \boldsymbol{M}_{\boldsymbol{d}}^{(1)} + \boldsymbol{M}_{\boldsymbol{d}}^{(2)} + \boldsymbol{M}_{\boldsymbol{f}},$

where subscripts f and d refer to the fuselage and duct contribution. $\boldsymbol{F}^{(j)}$ and $\boldsymbol{M}^{(j)}$ are instead the force and moment generated by the *j-th* main rotor. In particular, rotor forces are divided into three contributions: 1) aerodynamic, 2) inertial and 3) centrifugal. On the other hand, the main rotor moments are provided by their 1) aerodynamic, 2) inertial and 3) flap hinge stiffness components. Considering the single-blade contribution, of a $\Gamma-$rotating rotor (where $\Gamma = 1$ for a counter-clockwise rotor and $\Gamma = -1$ for a clockwise rotor) the aerodynamic force in hub-body frame of the i-th blade (subscript i) is computed as followings:

[3] $$\boldsymbol{F}_{\boldsymbol{a}_i} = \int_{r_c}^{R-e_0} R_{HB-bl}(\boldsymbol{dL} + \boldsymbol{dD})dr$$

where the infinitesimal force given by the sum of lift and drag, rotated from local blade to hub-body f.o.r. (rotation matrix R_{HB-bl}), is integrated along the blade span, from the root cutout (r_c) to the blade tip.

The infinitesimal lift and drag contributions at each blade section can be computed as

[4] $$\boldsymbol{dL} = \frac{1}{2}\rho c|\boldsymbol{V_a}|^2 C_L(\alpha_i, Re_i)\begin{bmatrix}\Gamma \sin\alpha_i \\ 0 \\ -\cos\alpha_i\end{bmatrix};$$

[5] $$\boldsymbol{dD} = \frac{1}{2}\rho c|\boldsymbol{V_a}|^2 C_D(\alpha_i, Re_i)\begin{bmatrix}-\Gamma \cos\alpha_i \\ 0 \\ -\sin\alpha_i\end{bmatrix}$$

where C_L and C_D are the aerodynamic lift and drag coefficients of the specific blade section subjected to a Reynolds number Re and an angle of attack α. Airfoil's aerodynamics is modelled by employing look-up tables of conventional NACA profiles and by extending them with semi-analytical formulas developed by Viterna [18]. $\boldsymbol{V_a}$ is the aerodynamic velocity at the blade section, which depends on the blade's orientation and the local inflow velocity (see Taamallah [8]).

On the other hand, the aerodynamic moment in the hub-body frame of the i-th blade is instead computed as an integral of the infinitesimal moments at each blade section, given by the cross product between the section position vector with respect to the hub centre and the aerodynamic force. In mathematical terms

[6] $$\boldsymbol{M}_{\boldsymbol{a}_i} = \int_{r_c}^{R-e_0} \boldsymbol{r} \times [R_{HB-bl}(\boldsymbol{dL} + \boldsymbol{dD})]\, dr$$

where $\boldsymbol{r}$ is the blade section's position vector in hub-body f.o.r. The expression of additional forces and moments, i.e. centrifugal, inertial, and flap hinge stiffness, are deeply described by Taamallah [8]. In general, for the *j-th* rotor,

[7] $\boldsymbol{F}^{(j)} = R_{B-HB} \sum_{i=1}^{N_b} (\boldsymbol{F}_{\boldsymbol{a}_i} + \boldsymbol{F}_{\boldsymbol{c}_i} + \boldsymbol{F}_{\boldsymbol{i}_i})$

[8] $\boldsymbol{M}^{(j)} = \boldsymbol{r}_{\boldsymbol{HB}}^{(j)} \times \boldsymbol{F}^{(j)} + R_{B-HB} \sum_{i=1}^{N_b} (\boldsymbol{M}_{\boldsymbol{a}_i} + \boldsymbol{M}_{\boldsymbol{s}_i} + \boldsymbol{M}_{\boldsymbol{i}_i})$

2.1.2 Rotor flap and lead-lag dynamics

The main rotor dynamics is described by the equations defining blade's flexibility. Blade's flap and lead-lag motions are considered in this analysis with a mathematical representation inspired by Taamalllah's work [19] on Pitch-Lag-Flap (P-L-F) articulated rotors. In that study, a Lagrangian method was applied to define a set of second order ordinary differential equations (ODE) which describe the coupled flap-lead-lag motion of the single blade. By defining the generalized forces acting on the blade element, Taamallah described the blade flexibility in a rotating f.o.r. In particular, for the i-th blade

[9] $\ddot{\beta}_i = \frac{1}{A_1}\left(-D_i^{\beta}\dot{\xi}_i + Q_i^{\beta} - F_i^{\beta}\right)$

[10] $\ddot{\xi}_i = \frac{1}{A_2}\left(-D_i^{\xi}\dot{\beta}_i + Q_i^{\xi} - F_i^{\xi}\right)$

where $A_1 = m_b \frac{(R-e_0)^2}{3}$ and $A_2 = m_b(e_F^2 + 2\, e_F\, r_G + \frac{(R-e_0)^2}{3})$ are defined as constants which depend on the inertia of the blade. The terms D_i^{β} and D_i^{ξ} are non-linear coupling terms whose expression can be found in [19] and are specific for the i-th blade. Similarly, the term $Q_i - F_i$ is the excitation of the ODE and represent the generalized force that creates the flap and lead-lag motion.

The above-presented flight dynamics model can be considered to give a good representation of vehicle flight dynamics throughout its operational envelope. However, when it comes to linearization and study of system's stability, this model formulation presents some criticalities. This is because the equations of motion are highly non-linear and include numerical integration into the Q terms. In addition, the rotating frame representation is suitable for the rotorcraft simulation but at the same time, loses physical meaning when studying the rotor stability and its regressive and advancing modes. The high level of coupling between rotor modes, make it unsuitable to study separately the effects of blade flexibility on rotorcraft stability. In order to overcome these problems, the equations are adapted and modified to represent the rotor dynamics in a non-rotating frame of reference (hub-body) and by partially decoupling the different modes.

Blade flap is described by the tip-path plane equations, while the lead-lag motion generates a dynamic variation of the rotor centre of gravity. By applying the Coleman representation for a 3-bladed rotor [20], the single blade flap and lead-lad angles are written in the following form:

[11] $\beta_i = a_0 - a_1 \cos\psi_i - b_1 \sin\psi_i$

[12] $\xi_i = \xi_0 - \xi_c \cos\psi_i - \xi_s \sin\psi_i$

where $\boldsymbol{\beta} = [a_0\ a_1\ b_1]$ are the coned-shape rotor coordinates (i.e. the coning angle a_0 and the lateral and longitudinal flap coordinates, a_1 and b_1) and $\boldsymbol{\xi} = [\xi_0\ \xi_c\ \xi_s]$ describe the motion of the rotor centre of gravity (i.e. collective ξ_0, and the advancing/regressive lag, ξ_c and ξ_s). The flap and lead-lag velocities and accelerations are transformed as well through an analytical derivation of equations [11] and [12]. In general, $\dot{\beta}_i$, $\ddot{\beta}_i$, $\dot{\xi}_i$ and $\ddot{\xi}_i$ are functions of the non-rotating coordinates, their derivatives and the angular velocity $\Omega = \dot{\psi}_i$.

By substituting equations [11 and [12 into equations [9 and [10, the rotor dynamics can be then expressed in hub-body f.o.r, as

[13] $\ddot{\boldsymbol{\beta}} = -K_1^{\beta}\dot{\boldsymbol{\beta}} - K_0^{\beta}\beta + C_1^{\beta}\dot{\boldsymbol{\xi}} + C_0^{\beta}\boldsymbol{\xi} + \boldsymbol{E}^{\boldsymbol{\beta}}$

[14] $\ddot{\boldsymbol{\xi}} = -K_1^{\xi}\dot{\boldsymbol{\xi}} - K_0^{\xi}\xi + C_1^{\xi}\dot{\boldsymbol{\beta}} + C_0^{\xi}\boldsymbol{\beta} + \boldsymbol{E}^{\xi}$

The expression of the K, C, and E terms can be found in Appendix B. In particular, K_0 and K_1 are constant matrices (at each time step) derived from the frame transformation, while C_0 and C_1 represent the coupling terms between flap and lead-lag dynamics. Those matrixes are highly non-linear, and an explicit transformation from a rotating to a non-rotating frame was not feasible. Indeed, they will be approximated by the Taylor expansion during the linearization process described below. $\boldsymbol{E}^{\boldsymbol{\beta}}$ and $\boldsymbol{E}^{\xi}$ are instead the excitation of the second order system, represented by the flapping and lead-lag moments computed with numerical integration. These two terms depend on the blade's azimuthal position, as well as its specific flap and lead-lag angles in a rotating frame and their velocities.

A second step to address the criticalities arisen from the original mathematical model representation is the partial decoupling of different modes. Indeed, the system in equations [13 and [14 still presents a strong coupling between the tip-path plane and rotor CG dynamics. Since one of the goals of this analysis is to be able to study separately the effects of flap and lead-lag on rotorcraft stability, a Simulink scheme was adopted to solve the two rotor modes by approximating the coupling and forcing terms with value of rotor flap and lead-lag coordinates at the previous time-step ($t - \Delta t$). The algorithm is depicted in Figure 3: Simulink scheme for partial decoupling of rotor flap and lead-lag dynamics.

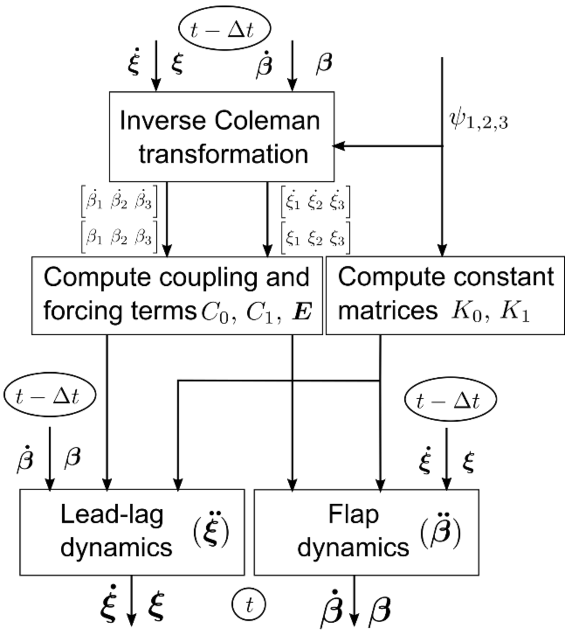

Figure 3: Simulink scheme for partial decoupling of rotor flap and lead-lag dynamics

In the algorithm, the blade positions (ψ_1, $\psi_2$and ψ_3) are used to compute the constant matrices K_0 and K_1 and transform the rotor coordinates in blade's angles. The calculation of the single blade flap and lead-lag angles is still necessary to compute the coupling and forcing terms of the equations, since a complete transformation from rotating to fixed f.o.r. is not feasible. The latter terms, together with the coupled rotor coordinates at the previous time-step, are used to solve equations for dynamic flap and lead-lag in hub-body frame (equations [13 and [14).

The algorithm allows to solve the equations in question and partially decouple them. In this way, one or the other dynamics can be excluded by simply cutting off its branch and studying the separate effects on the rotor.

2.2. Trim

A bottleneck of the analysis is the definition of a specific algorithm for the computation of the rotorcraft trim condition with the numerical modeling approach described in this work. Indeed, the problem cannot be solved simply by writing and solving a system of steady-state equations, since the forces and moments along the blades and the flap-lag moments are derived through numerical integration. In addition, the single-blade flap and lead-lag equations in the trim algorithm are written and solved in a rotating frame of reference, meaning that the solution depends on the current blade location. While a steady state solution of the rotor coordinates is expected to be found when modeling the trim with an analytical approach [21], this is not fully applicable in the present formulation. It has been observed that the tip-path plane and rotor CG coordinates depend on the starting blade location. Flap wobbling and rotor vibrations are observed during one revolution such that $\boldsymbol{\beta}$ and $\boldsymbol{\xi}$ change with time. Indeed, because of the presence of this rotor tilting motion, a general steady-state solution to the trim problem cannot be found if considering a unique blade configuration. Rotor forces and moments depend on the blade configurations and the TPP titling at each time step, making a solution found for single-blade configuration, not suitable to keep the rotorcraft in an equilibrium point in time. In order to find a condition that minimizes the average rotor acceleration in each blade ψ location, the trim has to be computed based on an average rotor force and moment on N_c number of symmetric blades' configurations. In general, considering $\boldsymbol{\psi_0} = [\psi_1\ \psi_2\ \psi_3]$ the vector containing the initial position of each blade, the k-th blades' configuration can be computed as

$$[15]\quad \boldsymbol{\psi_k} = \boldsymbol{\psi_0} + k\frac{2\pi}{N_b N_c}\ where\, k = 0,1,2,\ldots N_c - 1\,;$$

The trim algorithm is described in Figure 6: Trim algorithm. The solution to the problem is found by iteratively solving the steady-state coupled flap-lag equations, the steady-state 6 dof equations of motion (EoM), and the non-uniform steady-state inflow. It was observed that the algorithm cannot converge if solving those three blocks together, hence the iterations were split into an internal loop, which solves the EoM system and the steady inflow for fixed rotor coordinates, and an external loop which solves and update at each step the flap and lead-lag values. The algorithm works as follow:

- (a) starts with an initial condition of the 26 unknowns (6 flap coefficients, 6 lead-lag coefficients, 6 inflow coefficients, 2 collective pitch, 4 cyclic controls, roll and pitch angles);
- In (b-c) the steady state coupled flap and lead-lag system of equations is solved for each blade and the TPP and rotor CG coordinates are derived by applying Coleman transformation;
- (b-c) are repeated for N_c number of equally spaced blade configurations and the average value is computed in (d);
- in (e), knowing the average rotor coordinates, the main rotors forces and moments are computed with equations [7] $\boldsymbol{F}^{(j)} = R_{B-HB}\sum_{i=1}^{N_b}(\boldsymbol{F}_{\boldsymbol{a}_i} + \boldsymbol{F}_{\boldsymbol{c}_i} + \boldsymbol{F}_{\boldsymbol{i}_i})$[8] $\boldsymbol{M}^{(j)} = \boldsymbol{r}_{\boldsymbol{HB}}^{(j)} \times \boldsymbol{F}^{(j)} + R_{B-HB}\sum_{i=1}^{N_b}(\boldsymbol{M}_{\boldsymbol{a}_i} + \boldsymbol{M}_{\boldsymbol{s}_i} + \boldsymbol{M}_{\boldsymbol{i}_i})$. Again, (e) is repeated for N_c blade configurations, and the values are averaged around one revolution in (f).
- with the average values of rotor coordinates and main rotors forces and moments, the system of steady-state equations of motion is solved in (g). Two additional equations are added to take the control mix into account and close the system.
- in (h) the rotorcraft attitude and controls are used to update the non-uniform steady state inflow, derived from Peters' 3-states model [14];
- the internal loop (e-h) is repeated until a stopping criterion (maximum relative error between the rotorcraft state, inflow and controls at each internal iteration) is satisfied;
- once the internal loop has converged, rotorcraft state is updated, and a new external iteration is started. The external loop is repeated until a stopping criterion (maximum relative error between the TPP and rotor CG coordinates at each external iteration) is satisfied.

Attitude and control input results at trim for variable forward speed are reported in Figure 4: Trim attitude at variable forward speed and Figure 5: Trim controls at variable forward speed.

As expected, and by comparing the results with the analysis of Mazzeo *et al.* [15] carried on the same rotorcraft, the helicopter assumes a pitched down attitude as the forward speed increases, with a positive longitudinal cyclic input provided by the pilot (considered positive for a "push" effort). The collective pitch at hover is almost 10 degrees, while the lateral cyclic and differential longitudinal controls are almost zero. For the sake of this paper, only the hover condition will be studied by the linearization method, but the same procedure can be applied for every flight condition.

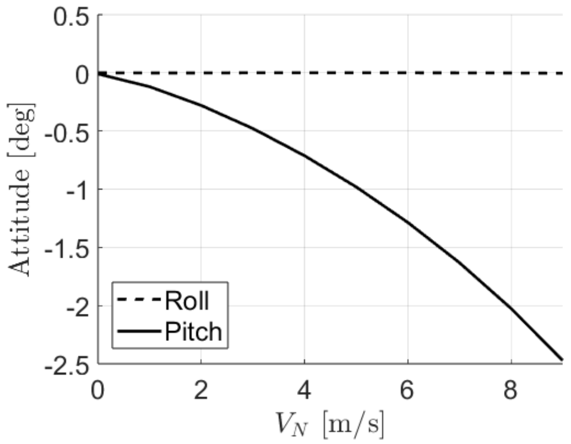

Figure 4: Trim attitude at variable forward speed

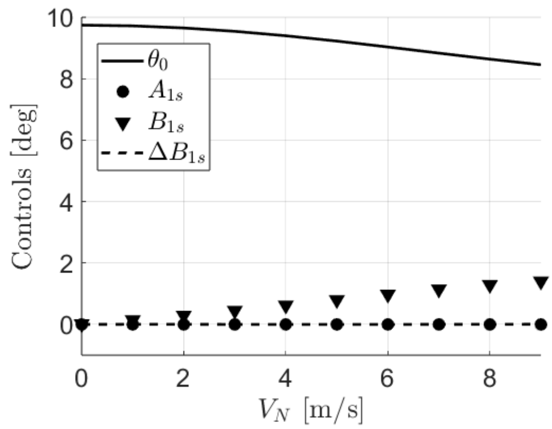

Figure 5: Trim controls at variable forward speed

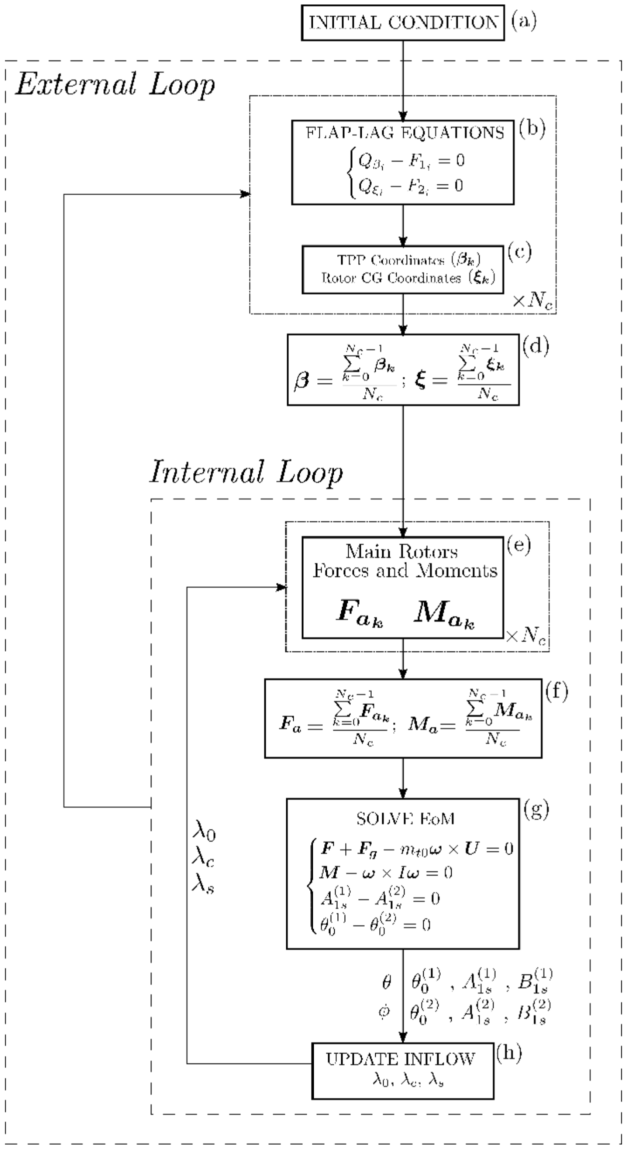

Figure 6: Trim algorithm

2.3. Linearization

In order to study the flight dynamic properties and open-loop stability of the rotorcraft, a numerical model has to be linearized around a specific trim condition. In this section, a methodology to compute a 38-state space linear model of the mathematical framework presented in Section 2.1 is presented. The system of ODEs describing the rigid body motion, rotor, and inflow dynamics is

$$[16] \quad \begin{cases} m_{t0}\dot{\boldsymbol{U}} = -m_{t0}\boldsymbol{\omega} \times \boldsymbol{U} + \boldsymbol{F_g} + \boldsymbol{F} \\ I\dot{\boldsymbol{\omega}} = \boldsymbol{M} - \boldsymbol{\omega} \times I\boldsymbol{\omega} \\ \ddot{\boldsymbol{\beta}} = \left[-K_1^{\beta}\dot{\boldsymbol{\beta}} - K_0^{\beta}\beta + C_1^{\beta}\dot{\boldsymbol{\xi}} + C_0^{\beta}\boldsymbol{\xi} + \boldsymbol{E^{\beta}}\right]^{(1/2)} \\ \ddot{\boldsymbol{\xi}} = \left[-K_1^{\xi}\dot{\boldsymbol{\xi}} - K_0^{\xi}\xi + C_1^{\xi}\dot{\boldsymbol{\beta}} + C_0^{\xi}\boldsymbol{\beta} + \boldsymbol{E^{\xi}}\right]^{(1/2)} \\ \dot{\boldsymbol{\lambda}}^{(1/2)} = \mathit{function}(\boldsymbol{x}) \end{cases}$$

where $\boldsymbol{\omega} = [p\ q\ r]$ and $\boldsymbol{U} = [u\ v\ w]$ are respectively the angular rate and rotorcraft velocity in body f.o.r. while $\boldsymbol{F_g}$ is the gravity force vector. The first six equations represent the 6 dof rigid body motion while the second twelve (6 for each rotor) are the second-order flap and lead-lag dynamics described in a non-rotating frame of reference. By applying a separation of variables, the rotor dynamics can be reduced to a set of 24 first-order ODEs, such that $\boldsymbol{d\beta} = [\dot{a}_0\ \dot{a}_1\ \dot{b}_1]$ and $\boldsymbol{d\xi} = [\dot{\xi}_0\ \dot{\xi}_c\ \dot{\xi}_s]$.

The system of equations has to be linearized and reduced to the form

$$[17] \quad \dot{\boldsymbol{x}} = A\boldsymbol{x} + B\boldsymbol{\tau}$$

where A, B, $\boldsymbol{x}$ and $\boldsymbol{\tau}$ are respectively the state and control matrices and the state and control vectors. In particular

$$[18] \quad \boldsymbol{x} = [u\ \ w\ \ q\ \ \theta\ \ v\ \ p\ \ \phi\ \ r\ \ \boldsymbol{\beta^{(1)}}\ \ \boldsymbol{\beta^{(2)}}\ \ \boldsymbol{d\beta^{(1)}}\ \ \boldsymbol{d\beta^{(2)}} \ldots$$

$$\ldots\ \boldsymbol{\xi^{(1)}}\ \ \boldsymbol{\xi^{(2)}}\ \ \boldsymbol{d\xi^{(1)}}\ \ \boldsymbol{d\xi^{(2)}}\ \ \boldsymbol{\lambda^{(1)}}\ \ \boldsymbol{\lambda^{(2)}}]$$

$$[19] \quad \boldsymbol{\tau} = [\theta_0\ \ A_{1s}\ \ B_{1s}\ \ \Delta B_{1s}]$$

The analytical expression of the state and control matrices (A and B) is derived by applying the small perturbation theory and manually compute the system's derivatives.

Consider a general state $x \in \boldsymbol{x} \cup \boldsymbol{\tau}$, this can be described as its trim condition x^0 plus an infinitely small perturbation δx, thus $x = x^0 + \delta x$. By substituting this approximation into equation [16, and by neglecting the second order terms ($O(\delta x^2)$), the system of equations can be written in terms of small perturbations. This describes the linear dynamics of the system around a specific trim condition.

In the numerical modelling approach, forcing and coupling terms of both rotor and rigid body equations are non-linear terms derived from the integration of single blade element contributions, which are themselves function of the rotorcraft state and controls. The external forces and moments ($\boldsymbol{F} = [X\ \ Y\ \ Z]$ and $\boldsymbol{M} = [L\ \ M\ \ N]$) and the excitation of rotor flap and lead-lag dynamics ($\boldsymbol{E^{\beta}}$ and $\boldsymbol{E^{\xi}}$**)** are the forcing terms of the respective ODEs. Those terms are represented by analytic functions of the disturbed motion variables and their derivatives using Taylor's expansion. They can be expressed as their trim value plus a sum of contributions from each state and control variable, such that

[20] $$\boldsymbol{F} = \boldsymbol{F^0} + \boldsymbol{F_u} u + \boldsymbol{F_w} w + \cdots + \boldsymbol{F_{\Delta B_{1s}}} \Delta B_{1s}$$

where the first-order derivative about the generic perturbation δx of the x state is computed numerically with a central finite difference formula as

[21] $$\boldsymbol{F}_x = \left.\frac{\partial \boldsymbol{F}}{\partial x_i}\right|_{x^0} = \frac{\boldsymbol{F}(x^0+\delta x)-\boldsymbol{F}(x^0-\delta x)}{2\delta x}$$

The same approach is also applied to the inflow equation and to the coupling terms in the rotor dynamics equations (C_0 and C_1). These terms are nonlinear terms representing the coupled effects between flap and lead-lag dynamics of each rotor. As it is impossible to rearrange these terms in an explicit form with the rotor states, the Taylor's approximation becomes a viable solution to produce a linearized model.

The state matrix A will indeed be a function of the trim condition and the stability derivatives which describe the linear response of the perturbed states. As a matter of fact, with the presented methodology, the stability of the system is described not only by the classical rigid body derivatives but also by the coupling body-rotor-inflow derivatives and the ones related to flap and lead-lag forcing and coupling terms. The general structure of the A matrix is the following

[22] $$A = \begin{bmatrix} A_B(8\times 38) \\ A_R(24\times 38) \\ A_\lambda(6\times 38) \end{bmatrix} = \begin{bmatrix} A_{B-B} & A_{B-R} & A_{B-\lambda} \\ A_{R-B} & A_{R-R} & A_{R-\lambda} \\ A_{\lambda-B} & A_{\lambda-R} & A_{\lambda-\lambda} \end{bmatrix}$$

where A_B, A_R and A_λ are respectively the linearized version of the rigid body, rotor, and inflow dynamics, and they are composed by a set of 3 sub-matrices for each of them.

Consider for example, the rigid body dynamics, the A_{B-B} matrix represents the 8-state linear model of the rigid body equations of motion (excluding the heading contribution), while A_{B-R} and $A_{B-\lambda}$ represent the coupling effect of the flap, lead-lag and inflow dynamics on the body motion. On the other hand, A_{R-B} matrix for example, represents the coupling effect of the rigid body motion on the rotor dynamics (flap and lead-lag).

While the expression of A_{B-B} matrix and the normalization of the stability derivatives can be found in Padfield [9], A_{B-R} (and similarly $A_{B-\lambda}$) is comprised by the stability derivatives derived by the total forces and moments, perturbed with a flap and lead-lag perturbation, i.e.

[23] $$A_{B-R} = \begin{bmatrix} X_{a_0^{(1)}} & X_{a_1^{(1)}} & X_{b_1^{(1)}} & \cdots & X_{\xi_0^{(1)}} & \cdots \\ Z_{a_0^{(1)}} & \cdots & \cdots & \cdots & Z_{\xi_0^{(1)}} & \cdots \\ M_{a_0^{(1)}} & \cdots & \cdots & \cdots & M_{\xi_0^{(1)}} & \cdots \\ 0 & \cdots & \cdots & \cdots & 0 & \cdots \\ Y_{a_0^{(1)}} & \cdots & \cdots & \cdots & Y_{\xi_0^{(1)}} & \cdots \\ L_{a_0^{(1)}} & \cdots & \cdots & \cdots & L_{\xi_0^{(1)}} & \cdots \\ 0 & \cdots & \cdots & \cdots & 0 & \cdots \\ N_{a_0^{(1)}} & \cdots & \cdots & \cdots & N_{\xi_0^{(1)}} & \cdots \end{bmatrix}$$

The flap and lead-lag dynamics, instead, are represented by the linearized version of the rotor dynamics equations, i.e. A_R matrix. Similarly to the body dynamics, A_R matrix contains of the pure rotor-rotor dynamics A_{R-R} plus the coupling effects of body and inflow on the rotor itself. The structure of matrix A_R is derived from the linearization of equations [13 and[14, by applying Taylor's theorem and finite differences to compute the stability derivatives representing the coupling and forcing terms of the equations. The analytical structure of A_R is reported in Appendix B. In the equation, the flap and lead-lag coupling coefficients C_0 and C_1 appear with their trim value ($C_0^{\beta,0}$) and with their variation under a general perturbed state ($C_{0_x}^{\beta}$). Similarly, the tip-path plane and rotor CG coordinates at trim (averaged around N_c configurations), affect the stability of the linearized system ($\boldsymbol{\beta^0}$ and $\boldsymbol{\xi^0}$). $\boldsymbol{E}_x^{\beta}$ and $\boldsymbol{E}_x^{\xi}$ are instead derivatives of the ODEs forcing terms, computed with respect to each term of the state and control vectors ($\boldsymbol{x}$ and $\boldsymbol{\tau}$). All the terms are derived for both rotors MR1 and MR2, such that, for example,

[24] $$K_0^{\beta} = \begin{bmatrix} K_0^{\beta,(1)} & \mathcal{Z}_{3\times 3} \\ \mathcal{Z}_{3\times 3} & K_0^{\beta,(2)} \end{bmatrix}$$

or, in the case of vectors,

[25] $$C_{0_x}^{\beta}\boldsymbol{\xi^0} + \boldsymbol{E}_x^{\beta} = \begin{bmatrix} C_{0_x}^{\beta,(1)}\boldsymbol{\xi}^{0,(1)} + \boldsymbol{E}_x^{\beta,(1)} \\ C_{0_x}^{\beta,(2)}\boldsymbol{\xi}^{0,(2)} + \boldsymbol{E}_x^{\beta,(2)} \end{bmatrix}$$

It can be observed that A_R is split, for the sake of clarity, into two matrixes: the first one depends exclusively on the trim condition, while the second depends on the stability derivatives computed for the coupling and forcing terms of rotor dynamics, perturbed with all the 38-states. In general, the i-th column of this matrix contains the derivatives computed for the i-th perturbed state or control variable, for both rotor 1 and rotor 2. A similar methodology is applied to the inflow dynamics to derive the linearized version of the inflow equations represented by matrix A_λ. More detailed expression for the linearized inflow equations can be found in Appendix B.

In order to study the open-loop stability of the rotorcraft, the analysis of the eigenvalues and eigenvectors of matrix A is performed. In general, 38 different poles will be identified and related to the rigid body, flap, lead-lag, and inflow dynamics, and the effects of different degrees of complexity are studied.

3. RESULTS AND DISCUSSION

3.1. Rigid body dynamics

The rigid body dynamics of the side-by-side helicopter in hovering conditions is studied by linearizing the system of ODEs in equation [16, with the described methodology. The analysis of the state matrix poles and eigenvectors reveals important information about the rotorcraft stability and dynamics behavior. A key aspect of this method is the capability to partially decouple the rotor modes and to study their effects separately. With this respect, Figure 7 shows the rigid body poles in the complex plane, in the case of a dynamic flap and uniform dynamic inflow ($\boldsymbol{\lambda} = [\lambda_0 \ \ 0 \ \ 0]$). The poles are listed, together with their frequency and damping, in Table 1. The effects of lead-lag and lateral/longitudinal inflow are neglected in this case and will be added separately. The identification of the poles is made by studying the mode participation of each rigid body eigenvector and by recalling classical aircraft nomenclature for rotorcraft eigenvalues.

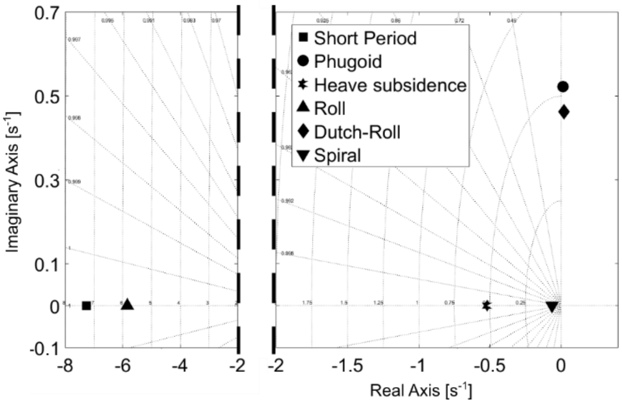

Figure 7: Rigid body poles in hovering condition with dynamic flap and and uniform inflow

The side-by-side helicopter dynamics is characterized by a couple of oscillatory, slightly unstable modes, which can be identified as low frequency, longitudinal and lateral modes, namely Phugoid and Dutch-Roll (also called Lateral Phugoid). Their behavior is characterized by the participation of the horizontal speed and pitch angle for the first and lateral speed coupled with roll angle and yaw rate for the second (Figure 9 and Figure 12). A couple of real and stable poles, characterize the high-frequency dynamics, namely short period and roll modes. These two poles are characterized by the main contribution of the pitch and roll rate respectively, together with a smaller participation of the pitch and roll angles and the longitudinal and lateral speed Figure 8 and Figure 11. In addition, it has been observed that, for this configuration, the lateral dynamics is always coupled with the yaw rate. Finally, a couple of low frequency, stable, poles is identified as heave-subsidence and spiral modes, as there are characterized by their typical mode participation: vertical velocity and yaw rate plus lateral speed (Figure 10 and Figure 13).

Mode	Pole	Freq.	Damp.
Short period	-7.26	7.26	-
Phugoid	0.013 ± 0.52i	0.52	0.024
Heave subsidence	-0.52	0.52	-
Roll	-5.84	5.84	-
Dutch-Roll	0.021 ± 0.46i	0.46	0.045
Spiral	-0.064	0.064	-

Table 1: Rigid body poles, frequency (in s^{-1}) and damping with a dynamic flap and uniform inflow

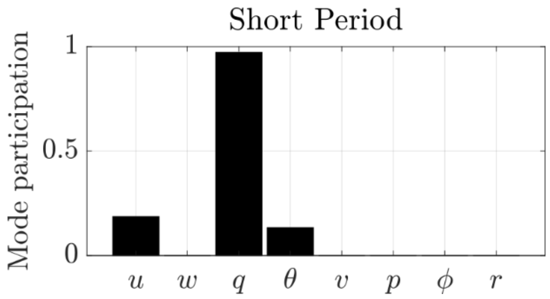

Figure 8: Short period mode

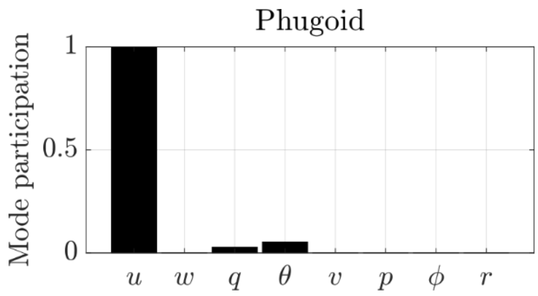

Figure 9: Phugoid mode

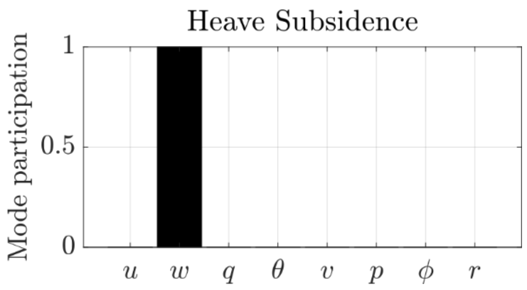

Figure 10: Heave subsidence mode

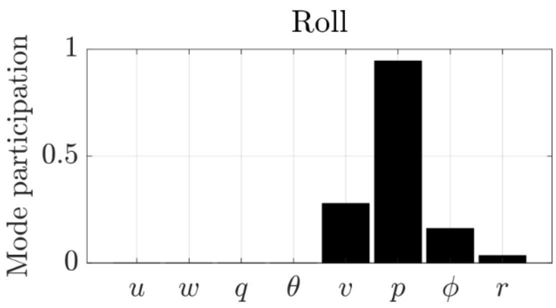

Figure 11: Roll mode

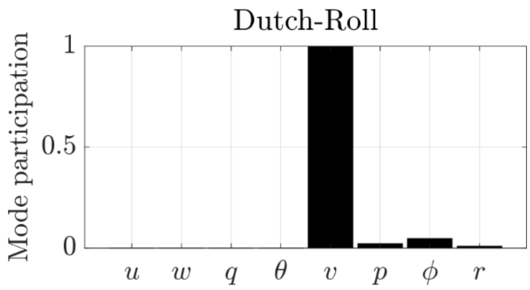

Figure 12: Dutch-Roll mode

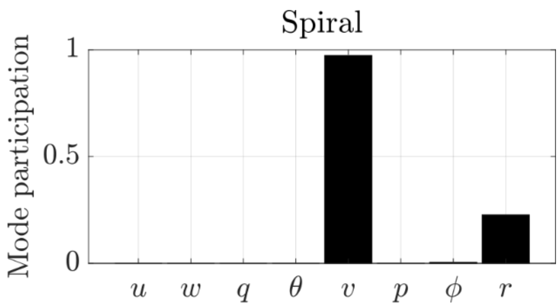

Figure 13: Spiral mode

An additional degree of complexity modeled in the numerical framework is the blade lead-lag dynamics. Blade's in-plane flexibiliy allows for an advancing and regressive lead-lag mode which is equivalent with a rotor CG motion in the rotor in-plane direction, caused by the leading or lagging of the blades during their rotation. The effect of this movement on the stability of the system is reported in Figure 14 and Table 2 with the representation of the rigid body poles in the case of lagging blades. While a small stabilizing effect is observed on the oscillatory modes (phugoid and dutch-roll), very small changes are observed in the frequency of the low-frequency poles. On the other hand, roll and short period are much more affected by the presence of the lead-lag, as the frequency of these two stable and real dynamics moves, respectively, from 5.84 to 10.7 s^{-1} and from 7.26 to 15 s^{-1}. The reason behind this effect is related to the coupling between the tip path plane and rotor center of gravity dynamics. Indeed, the lead-lag angle is not directly responsible for an additional force/moment acting on the blades but affects the value of the flap. Table 2 reports the values of rotor disc tilt and CG coordinates with a pitch perturbation $\Delta q = 0.01$ rad/s and the damping derivatives with and without lead-lag. It is observed that, while b_1 is similar in the two cases, a_1 significantly changes in the case of coupled lead-lag dynamics. The latter affects the absolute value of hinge stiffness and inertial moments (see equations

[1] and [2]) and increases the longitudinal damping derivative M_q (main responsible for the short period damping). The same process occurs with a roll rate perturbation Δp, and the L'_p derivative (main responsible for the roll damping).

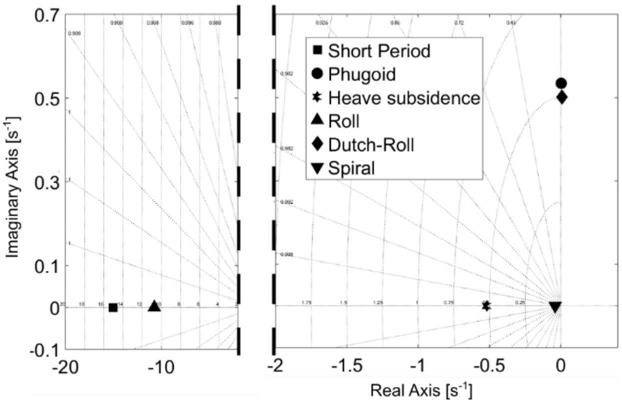

Figure 14: Rigid body poles in hovering condition with dynamic flap and lead-lag, and uniform inflow

Mode	Pole	Freq.	Damp.
Short period	-15.0	15.0	-
Phugoid	0.0032±0.53i	0.53	0.0059
Heave subsidence	-0.52	0.52	-
Roll	-10.72	10.72	-
Dutch-Roll	0.0078±0.50i	0.50	0.016
Spiral	-0.039	0.039	-

Table 2: Rigid body poles, frequency (in s^{-1}) and damping with a dynamic flap and lead-lag, and uniform inflow

		Only flap	Coupled flap-lag
$a_0(\Delta q = 0.01)$	[deg]	0.53	0.69
$a_1(\Delta q = 0.01)$	[deg]	-0.0047	-0.023
$b_1(\Delta q = 0.01)$	[deg]	0.014	0.013
M_q	-	-7.2	-15
L'_p	-	-5.8	-10.7

Table 3: Effect of lead-lag on tip-path plane coordinates with a perturbed pitch rate $\Delta q = 0.01$ rad/s and damping derivatives.

The last, and highest level of complexity can be achieved by adding a non-uniform inflow model, i.e. by considering, for both rotors, $\boldsymbol{\lambda} = [\lambda_0\ \lambda_s\ \lambda_c]$. Figure 15: Rigid body poles in hovering condition with dynamic flap,lead-lag, and non uniform inflow and Table 4 represents the rigid body poles in the case of non-uniform dynamic inflow, with complete flap and lead-lag dynamics. Three different x-axis scaling represent the low, high, and very high-frequency poles in the complex plane. The very high frequency plot is used to represent the inflow poles derived from the 38-state linearization method. Those six poles (three per rotor) are real and stable dynamics representing the uniform inflow at 33.5 rad/s and the lateral/longitudinal inflow modes at 126 rad/s (0.5/rev). It is observed that the lateral and longitudinal inflow components couple with the short period, dutch-roll, phugoid and roll dynamics. Considering the first one, an increase of the longitudinal damping is observed, linked to the mode coupling between short period and longitudinal inflow λ_c (see Figure 16 for the mode participation).

A similar coupling effect which is highly detrimental to rotorcraft stability, is the one between the longitudinal inflow and the phugoid modes. Even with a smaller mode participation, the longitudinal inflow contribution has the effect of "moving" the phugoid poles from a pure oscillatory, slightly unstable, situation, to a couple of real stable/unstable poles of similar frequency (Figure 18). On the other hand, the dutch-roll stability remains unchanged although its frequency decreases by about 50%. Coupling with both lateral and longitudinal inflows is observed in the dutch-roll and roll poles as well, although without significant changes in the lateral stability. It can be assumed that being the configuration symmetrical with respect to the longitudinal plane, the effect of the lateral inflows of the two rotors balances themselves, while the longitudinal contribution is detrimental to the low-frequency longitudinal stability.

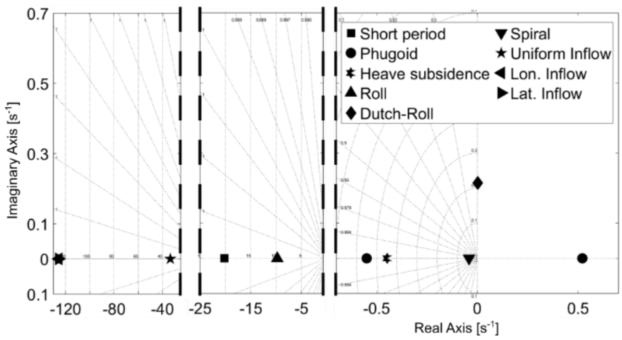

Figure 15: Rigid body poles in hovering condition with dynamic flap,lead-lag, and non uniform inflow

Mode	Pole	Freq.	Damp.
Short period	-20.2	20.2	-
Phugoid (+)	0.52	0.52	-
Phugoid (-)	-0.55	0.55	-
Heave subsidence	-0.45	0.45	-
Roll	-9.78	9.78	-
Dutch-Roll	0.0029±0.22	0.22	0.014
Spiral	-0.041	0.041	-

Table 4: Rigid body poles, frequency (in s-1) and damping with dynamic flap, lead-lag, and non uniform inflow

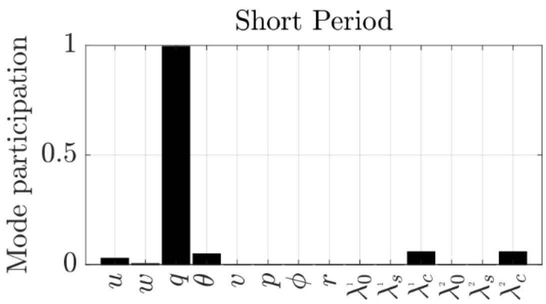

Figure 16: Short period mode, coupled with non uniform inflow

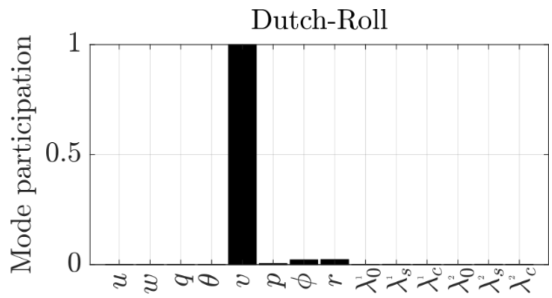

Figure 17: Dutch-roll mode, coupled with non uniform inflow

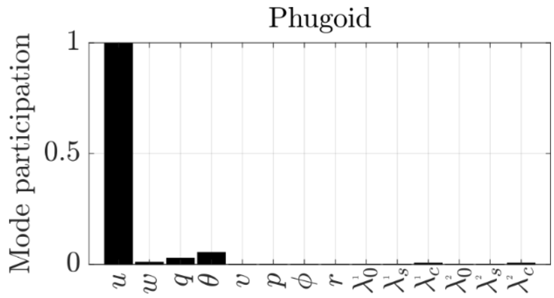

Figure 18: Phugoid mode, coupled with non uniform inflow

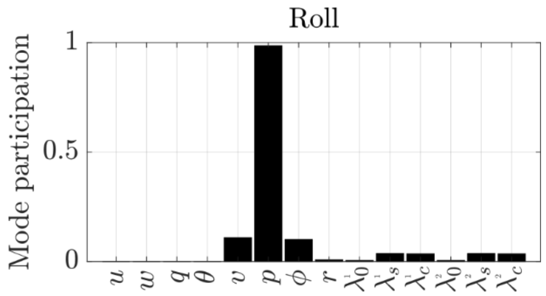

Figure 19: Roll mode, coupled with non uniform inflow

3.2. Rotor dynamics

The linearization method presented in this paper allows for developing a 38-state space representation of the rotorcraft flight dynamics, including the rigid body, rotor, and inflow modes. The out-of-diagonal submatrices of the state matrix A describe the coupling between the three dynamics in the side-by-side helicopter case, while A_{B-B}, A_{R-R}, and $A_{\lambda-\lambda}$ represent the pure dynamic effects. In this section, the rotor-rotor modes are studied and represented for one single rotor. It is observed that no differences occur, in hovering conditions, between rotor MR1 and MR2, and no particular coupling is present.

A set of 12 rotor poles is computed for each rotor, 3 of them linked to pure flap dynamics, 3 for the lead-lag, and 6 representing the strong coupling between those two dynamics. Figure 20 shows the mode participation of the 6, pure oscillatory, poles, representing the coupling effects between flap and lead-lag. Two complex conjugate poles represent the coupling between the dynamic coning angle (a_0) and the collective lead-lag (ξ_0). These two poles have an oscillating frequency of $\omega_0 = 4.55$ rad/s (Table 5), which is approximately 0.02Ω. The other 4 poles are a combination of lateral/longitudinal disc tilts (a_1 and b_1), advancing and regressive rotor CG coordinates (ξ_c and ξ_s), and their first-order derivatives. The higher frequency modes are called "coupled advancing modes", while the lower frequency ones are the "coupled regressive modes". These coupled dynamics are purely oscillatory and located at a frequency of $\omega_0 \pm \Omega$ (Table 5).

Figure 21 and Figure 22 show the mode participation of the purely flap and lead-lag dynamics. These two sets of 3 poles are made of a real pole located in the origin (Table 5), at zero frequency, only participated by the coning (a_0) or the collective lead-lag (ξ_0), and a couple of complex conjugate poles at the rotor angular frequency Ω (Table 5). The latter represent the non-uniform disc tilt and lead-lag motions but cannot be reduced to classical advancing or regressive modes. Indeed, while a major contribution of flap and lead-lag components is highlighted, no frequency differences are observed.

Mode	Pole [rad/s]
Coupled collective mode	± 4.55i
Coupled advancing mode	± 256i
Coupled regressive mode	± 247i
Collective flap	0
Non-uniform disc tilt	± 251i
Collective lead-lag	0
Non-uniform lead-lag	± 251i

Table 5: Rotor poles

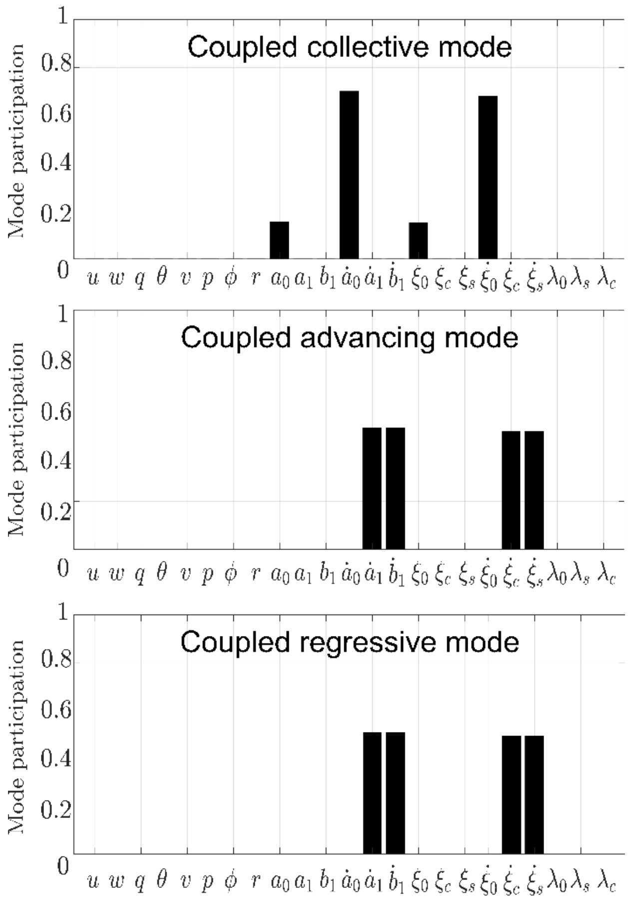

Figure 20: Mode participation of the rotor coupled poles

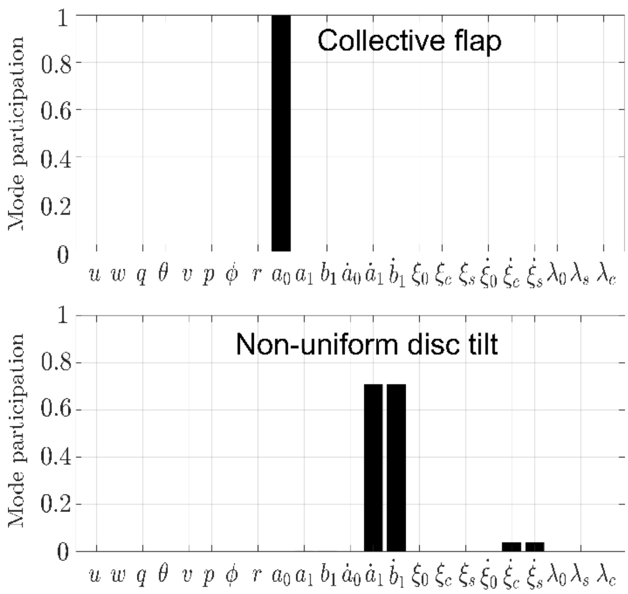

Figure 21: Mode participation of the rotor flap poles

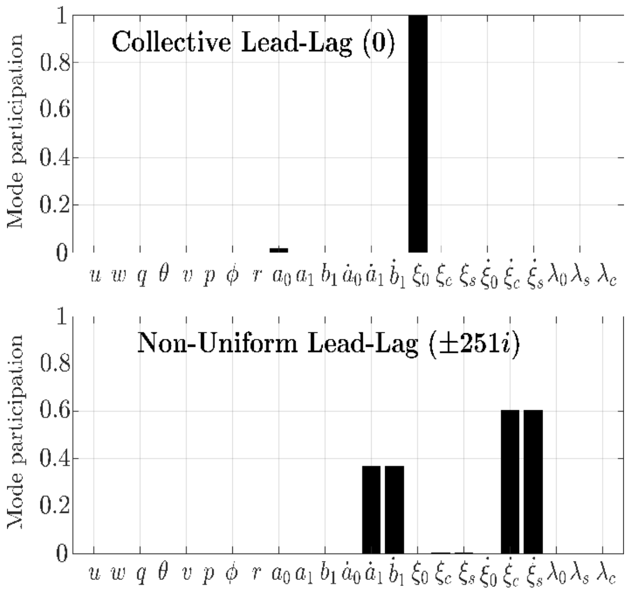

Figure 22: Mode participation of the rotor lead-lag poles

4. CONCLUSIONS

This paper proposed a methodology for linearizing highly coupled numerical models applied on a side-by-side helicopter. To this aim, a 24 dof, mathematical representation of rotorcraft flight dynamics was obtained by integrating second-order flap and lead-lag dynamics, with a non-uniform, first-order, dynamic inflow and integral computation of single blade forces and moments.

In order to compute the trim conditions, an iterative algorithm made of two nested loops has been derived by averaging the solution of rotor forces, moments and blade's flexibility around one revolution. Trim curves at variable forward speed are produced and the hovering solution is selected for flight dynamic studies. A methodology to linearize the system of ODEs representing the 24 dof of the rotorcraft, around the hovering condition, is presented:

- Flap and lead-lag dynamics have been partially decoupled by rearranging the equations in a non-rotating frame of reference and by adopting a Simulink algorithm to solve the two dynamics separately. This allows for isolating the effects of blade's flexibility on rotorcraft stability a provide physical meaning to the linear representation.
- An analytical form of the state matrix has been derived, including body-rotor-inflow coupling effects and rotor dynamics.
- Nonlinear and integral terms in the equations have been treated with Taylor's expansion and a set of stability derivatives representing the rotor coupling have been derived manually.

As a result of the linearization method applied to the side-by-side helicopter case, the flight dynamics properties and stability of the rotorcraft are assessed, and the effects of single rotor dynamics have been isolated and studied separately. The rotorcraft is subjected to a couple of unstable oscillatory modes, governed by the pitch and roll angles, identified as classical phugoid and Dutch-roll modes. A couple of high-frequency, real and stable poles representing the short period and roll modes are identified, as well as low frequency and stable, heave subsidence and spiral behaviors.

It is observed that a stabilizing effect is introduced by the lead-lag, especially on the high-frequency poles. On the other hand, the coupling between the rigid body modes and a non-unifom inflow representation, leads to dangerous and unstable phugoid, as well as a reduction of Dutch-roll damping.

Rotor dynamics has been addressed as well, by showing the presence of coupled flap-lead-lag poles which behave as collective, advancing and regressive oscillatory, high-frequency, modes.

In conclusion, the presented methodology can be applied to any numerical framework representing the flight dynamics of multiple helicopter configurations. The trim and stability properties are computed, and a linear 38-state-space representation of the side-by-side helicopter flight dynamics has been provided.

Appendix A

Description	Symbol	Value
Maximum Take-Off Mass [kg]	m_{t0}	20.62
Inertia matrix wrt $[x_B\ y_B\ z_B]$ [kg m²]	I	$\begin{bmatrix} 3.532 & -0.001 & -0.052 \\ -0.001 & 2.222 & 0 \\ -0.052 & 0 & 5.342 \end{bmatrix}$
Rotors		
Sense of rotation	Γ	± 1
Number of blades	N_b	3
Radius [m]	R	0.505 0.051
Mean chord [m]	c	0.0964 2400 0.075
Solidity ratio [-]	σ	0.0075 0.1613
Angular velocity [rpm]	Ω	3
Total hinge offset [m]	e_0	0.505 0.051
Flap hinge offset [m]	e_F	0.0964 2400 0.075
Blade mass [kg]	m_b	0.0075 0.1613
Blade's center of gravity wrt the hub [m]	r_G	0.224
Spring restraint coefficient due to flap [Nm/rad]	$K_{s\beta}$	162
Spring restraint coefficient due to lead-lag [Nm/rad]	$K_{s\xi}$	0
Pitch-Flap coupling ratio [-]	$K_{t\beta}$	0
Pitch-Lag coupling ratio [-]	$K_{t\xi}$	0
Blade's constant twist coefficient [rad]	θ_w	0
Longitudinal incidence angle [rad]	i_s	0
Lateral incidence angle [rad]	i_c	0
Hub position of the MR1 wrt body axes [m]	$\boldsymbol{r}_{\boldsymbol{HB}}^{(\mathbf{1})}$	[0 -0.645 0.066]
Hub position of the MR2 wrt body axes [m]	$\boldsymbol{r}_{\boldsymbol{HB}}^{(\mathbf{2})}$	[0 0.645 0.066]

Table 6: Side-by-side helicopter data

Appendix B

The rotor flap and lead-lag dynamics represented in a non-rotating frame of reference in equations [13 and [14 depends on the following terms:

[26] $$K_1^\beta = \begin{bmatrix} 1 & -\cos\psi_1 & -\sin\psi_1 \\ 1 & -\cos\psi_2 & -\sin\psi_2 \\ 1 & -\cos\psi_3 & -\sin\psi_3 \end{bmatrix}^{-1} \begin{bmatrix} 0 & 2\Omega\sin\psi_1 & -2\Omega\cos\psi_1 \\ 0 & 2\Omega\sin\psi_2 & -2\Omega\cos\psi_2 \\ 0 & 2\Omega\sin\psi_3 & -2\Omega\cos\psi_3 \end{bmatrix}$$

[27] $$K_0^\beta = \begin{bmatrix} 1 & -\cos\psi_1 & -\sin\psi_1 \\ 1 & -\cos\psi_2 & -\sin\psi_2 \\ 1 & -\cos\psi_3 & -\sin\psi_3 \end{bmatrix}^{-1} \begin{bmatrix} 0 & \Omega^2\cos\psi_1 + \dot{\Omega}\sin\psi_1 & \Omega^2\sin\psi_1 - \dot{\Omega}\cos\psi_1 \\ 0 & \Omega^2\cos\psi_2 + \dot{\Omega}\sin\psi_2 & \Omega^2\sin\psi_2 - \dot{\Omega}\cos\psi_2 \\ 0 & \Omega^2\cos\psi_3 + \dot{\Omega}\sin\psi_3 & \Omega^2\sin\psi_3 - \dot{\Omega}\cos\psi_3 \end{bmatrix}$$

For the sake of this paper, Coleman transformation is applied for both flap and lead-lag, meaning that $K_1^{\xi} = K_1^{\beta}$ and $K_0^{\xi} = K_0^{\beta}$.

[28] $$C_1^{\beta} = \frac{1}{A_1}\begin{bmatrix}1 & -\cos\psi_1 & -\sin\psi_1\\ 1 & -\cos\psi_2 & -\sin\psi_2\\ 1 & -\cos\psi_3 & -\sin\psi_3\end{bmatrix}^{-1}\begin{bmatrix}-D_1^{\beta} & 0 & 0\\ 0 & -D_2^{\beta} & 0\\ 0 & 0 & -D_3^{\beta}\end{bmatrix}\begin{bmatrix}1 & -\cos\psi_1 & -\sin\psi_1\\ 1 & -\cos\psi_2 & -\sin\psi_2\\ 1 & -\cos\psi_3 & -\sin\psi_3\end{bmatrix}$$

[29] $$C_0^{\beta} = \frac{1}{A_1}\begin{bmatrix}1 & -\cos\psi_1 & -\sin\psi_1\\ 1 & -\cos\psi_2 & -\sin\psi_2\\ 1 & -\cos\psi_3 & -\sin\psi_3\end{bmatrix}^{-1}\begin{bmatrix}-D_1^{\beta} & 0 & 0\\ 0 & -D_2^{\beta} & 0\\ 0 & 0 & -D_3^{\beta}\end{bmatrix}\begin{bmatrix}0 & \Omega\sin\psi_1 & -\Omega\cos\psi_1\\ 0 & \Omega\sin\psi_2 & -\Omega\cos\psi_2\\ 0 & \Omega\sin\psi_3 & -\Omega\cos\psi_3\end{bmatrix}$$

[30] $$C_1^{\xi} = \frac{1}{A_2}\begin{bmatrix}1 & -\cos\psi_1 & -\sin\psi_1\\ 1 & -\cos\psi_2 & -\sin\psi_2\\ 1 & -\cos\psi_3 & -\sin\psi_3\end{bmatrix}^{-1}\begin{bmatrix}-D_1^{\xi} & 0 & 0\\ 0 & -D_2^{\xi} & 0\\ 0 & 0 & -D_3^{\xi}\end{bmatrix}\begin{bmatrix}1 & -\cos\psi_1 & -\sin\psi_1\\ 1 & -\cos\psi_2 & -\sin\psi_2\\ 1 & -\cos\psi_3 & -\sin\psi_3\end{bmatrix}$$

[31] $$C_0^{\xi} = \frac{1}{A_2}\begin{bmatrix}1 & -\cos\psi_1 & -\sin\psi_1\\ 1 & -\cos\psi_2 & -\sin\psi_2\\ 1 & -\cos\psi_3 & -\sin\psi_3\end{bmatrix}^{-1}\begin{bmatrix}-D_1^{\xi} & 0 & 0\\ 0 & -D_2^{\xi} & 0\\ 0 & 0 & -D_3^{\xi}\end{bmatrix}\begin{bmatrix}0 & \Omega\sin\psi_1 & -\Omega\cos\psi_1\\ 0 & \Omega\sin\psi_2 & -\Omega\cos\psi_2\\ 0 & \Omega\sin\psi_3 & -\Omega\cos\psi_3\end{bmatrix}$$

The linearized rotor dynamics is expressed by

[32] $$A_R = \begin{bmatrix} & \mathcal{Z}_{6\times6} & \mathcal{I}_6 & \mathcal{Z}_{6\times6} & \mathcal{Z}_{6\times6} & \\ \mathcal{Z}_{24\times8} & -K_0^{\beta} & -K_1^{\beta} & C_0^{\beta,0} & C_1^{\beta,0} & \mathcal{Z}_{24\times6} \\ & \mathcal{Z}_{6\times6} & \mathcal{Z}_{6\times6} & \mathcal{Z}_{6\times6} & \mathcal{I}_6 & \\ & -K_0^{\xi} & -K_1^{\xi} & C_0^{\xi,0} & C_1^{\xi,0} & \end{bmatrix} + \begin{bmatrix}\mathcal{Z}_{6\times1} & \cdots\\ C_{0_x}^{\beta}\boldsymbol{\xi}^{\mathbf{0}} + \boldsymbol{E}_x^{\beta} & \cdots\\ \mathcal{Z}_{6\times1} & \cdots\\ C_{0_x}^{\xi}\boldsymbol{\beta}^{\mathbf{0}} + \boldsymbol{E}_x^{\xi} & \cdots\end{bmatrix}$$

where $\mathcal{Z}_{i\times j}$ is a zero matrix of dimensions $i \times j$, while $\mathcal{I}_i$ is an identity matrix of dimensions $i \times i$.

The same approach of the rotor dynamics is adopted for the inflow dynamics. Assuming a general expression of the inflow equation $\dot{\boldsymbol{\lambda}} = C^{\lambda}\boldsymbol{\lambda} + \boldsymbol{E}^{\boldsymbol{\lambda}}$, where $\boldsymbol{\lambda} = [\lambda_0\ \ \lambda_c\ \ \lambda_s]$, the linearized matrices can be found as

[33] $$A_{\lambda-\lambda}(6\times6) = \begin{bmatrix}C^{\lambda,0,(1)} & 0\\ 0 & C^{\lambda,0,(2)}\end{bmatrix} + \begin{bmatrix}C_{\lambda_0}^{\lambda,(1)}\boldsymbol{\lambda}^{\mathbf{0},(1)} + \boldsymbol{E}_{\lambda_0}^{\boldsymbol{\lambda},(1)} & C_{\lambda_c}^{\lambda,(1)}\boldsymbol{\lambda}^{\mathbf{0},(1)} + \boldsymbol{E}_{\lambda_c}^{\boldsymbol{\lambda},(1)} & C_{\lambda_s}^{\lambda,(1)}\boldsymbol{\lambda}^{\mathbf{0},(1)} + \boldsymbol{E}_{\lambda_s}^{\boldsymbol{\lambda},(1)}\\ C_{\lambda_0}^{\lambda,(2)}\boldsymbol{\lambda}^{\mathbf{0},(\mathbf{2})} + \boldsymbol{E}_{\lambda_0}^{\boldsymbol{\lambda},(2)} & C_{\lambda_c}^{\lambda,(2)}\boldsymbol{\lambda}^{\mathbf{0},(2)} + \boldsymbol{E}_{\lambda_c}^{\boldsymbol{\lambda},(2)} & C_{\lambda_s}^{\lambda,(2)}\boldsymbol{\lambda}^{\mathbf{0},(2)} + \boldsymbol{E}_{\lambda_s}^{\boldsymbol{\lambda},(2)}\end{bmatrix}$$

where superscripts 0 indicate trim condition, (1) and (2) indicate the main rotor and the subscripts indicate with respect to which state the derivative is calculated. Similarly, both $A_{\lambda-B}(6\times8)$ and $A_{\lambda-R}(6\times24)$ are computed as

[34] $$A_{\lambda-B,R} = \begin{bmatrix}C_x^{\lambda,(1)}\boldsymbol{\lambda}^{\mathbf{0},(1)} + \boldsymbol{E}_x^{\boldsymbol{\lambda},(1)} & \cdots\\ C_x^{\lambda,(2)}\boldsymbol{\lambda}^{\mathbf{0},(\mathbf{2})} + \boldsymbol{E}_x^{\boldsymbol{\lambda},(2)} & \cdots\end{bmatrix}$$

REFERENCES

[1] I. Levitt, N. Phojanamongkolkij, A. Horn, e K. Witzberger, «UAM Airspace Research Roadmap - Rev. 2.0», mar. 2023. Accessed on: 4 July 2024. [Online]. Available at: https://ntrs.nasa.gov/citations/20230002647

[2] R. K. Heffley e M. A. Mnich, «Minimum-complexity helicopter simulation math model - NASA Technical Reports Server (NTRS)». Accessed on: 6 February 2024. [Online]. Available at: https://ntrs.nasa.gov/citations/19880020435

[3] P. D. Talbot, B. E. Tinling, W. A. Decker, e R. T. N. Chen, «A mathematical model of a single main rotor helicopter for piloted simulation», NAS 1.15:84281, set. 1982. Accessed on: 10 February 2023. [Online]. Available at: https://ntrs.nasa.gov/citations/19830001781

[4] «FLIGHTLABTMmodeling for real-time simulation applications | International Journal of Modeling, Simulation, and Scientific Computing». Accessed on: 4 July 2024. [Online]. Available at: https://www.worldscientific.com/doi/abs/10.1142/S1793962317430036

[5] A. Savino, A. Cocco, A. Zanotti, M. Tugnoli, P. Masarati, e V. Muscarello, «Coupling Mid-Fidelity Aerodynamics and Multibody Dynamics for the Aeroelastic Analysis of Rotary-Wing Vehicles», *Energies*, vol. 14, fasc. 21, Art. fasc. 21, Jan. 2021, doi: 10.3390/en14216979.

[6] E. Quon, M. Smith, G. Whitehouse, e D. Wachspress, «Hierarchical Variable Fidelity Methods for Rotorcraft Aerodynamic Design and Analysis», presented at American Helicopter Society 67th Annual Forum, Virginia Beach, Virginia, USA, 2011.

[7] J. J. Howlett, «UH-60A Black Hawk engineering simulation program. Volume 1: Mathematical model», SER-70452, Dec. 1981. Accessed on: 4 July 2024. [Online]. Available at: https://ntrs.nasa.gov/citations/19840020737

[8] S. Taamallah, «A Flight Dynamics Model for a Small-Scale Flybarless Helicopter», *J. Dyn. Syst. Meas. Control*, vol. 138, fasc. 1, Nov. 2015, doi: 10.1115/1.4031738.

[9] G. D. Padfield, *Helicopter Flight Dynamics: The Theory and Application of Flying Qualities and Simulation Modelling*. John Wiley & Sons, 2008.

[10] M. A. Diftler, «UH-60A HELICOPTER STABILITY AUGMENTATION STUDY».

[11] B. L. Aponso, D. E. Johnston, W. A. Johnson, e R. E. Magdaleno, «Identification of Higher Order Helicopter Dynamics Using Linear Modeling Methods», *J. Am. Helicopter Soc.*, vol. 39, fasc. 3, pp. 3–11, Jul. 1994, doi: 10.4050/JAHS.39.3.3.

[12] S. R. Thrnour e R. Celi, «Effects of blade flexibility on helicopter stability and frequency response», presentato al 19th European Rotorcraft Forum, 1993.

[13] «Home | SAB Group | Emilia-Romagna», Sabgroup. Accessed on: 18 July 2024. [Online]. Available at: https://www.sabgroup.it

[14] D. A. Peters e N. Haquang, «Dynamic inflow for practical applications», *Am. Helicopter Soc. J.*, vol. 33, ott. 1988, Accessed on: 10 February 2023. [Online]. Available at: https://ntrs.nasa.gov/citations/19890032254

[15] F. Mazzeo, M. D. Pavel, D. Fattizzo, G. Bertolani, E. L. de Angelis, e F. Giulietti, «Flight dynamic modeling and stability of a small-scale side-by-side helicopter for Urban Air Mobility», *Aerosp. Sci. Technol.*, vol. 148, p. 109117, May 2024, doi: 10.1016/j.ast.2024.109117.

[16] B. N. Bourtsev e S. V. Selemenev, «Fan – in – Fin Performance at Hover Computational Method».

[17] G. J. Leishman, *Principles of Helicopter Aerodynamics*. Cambridge University Press, 2006.

[18] L. A. Viterna e D. C. Janetzke, «Theoretical and experimental power from large horizontal-axis wind turbines», Sep. 1982, doi: 10.2172/6763041.

[19] S. Taamallah, «Small-Scale Helicopter Blade Flap-Lag Equations of Motion for a Flybarless Pitch-Lag-Flap Main Rotor», in *AIAA Modeling and Simulation Technologies Conference*, Portland, Oregon: American Institute of Aeronautics and Astronautics, Aug. 2011. doi: 10.2514/6.2011-6279.

[20] R. P. Coleman e A. M. Feingold, «Theory of self-excited mechanical oscillations of helicopter rotors with hinged blades». 1 January 1958. Accessed on: 6 February 2024. [Online]. Available at: https://ntrs.nasa.gov/citations/19930092339

[21] R. W. Prouty, *Helicopter Performance, Stability, and Control*. R.E. Krieger Publishing Company, 1995.

Authors contacts:

Francesco Mazzeo, francesco.mazzeo@unimore.com , Via P.Vivarelli, 10, Modena (MO), 41125, Italy

Marilena D. Pavel, m.d.pavel@tudelft.nl , Kluyverweg 1, Delft, 2629HS, The Netherlands

Francesco Leali, fleali@unimore.it , Via P.Vivarelli, 10, Modena (MO), 41125, Italy

Fabrizio Giulietti, fabrizio.giulietti@unibo.it , Via Fontanelle, 40, Forlì (FC), 47121, Italy

Acknowledgments

The authors acknowledge and thank the company SABGroup S.R.L. for providing the rotorcraft's prototype and sharing constructive data. This study was carried out within the MOST - Sustainable Mobility National Research Center and received funding from the European Union Next-GenerationEU (PIANO NAZIONALE DI RIPRESA E RESILIENZA (PNRR) - MISSIONE 4 COMPONENTE 2, INVESTIMENTO 1.4 - D.D. 1033 17/06/2022, CN00000023). This manuscript reflects only the authors' views and opinions, neither the European Union nor the European Commission can be considered responsible for them.